Title
Pathways for the Photoreduction of Fumarate on ZnS

Journal
ACS Earth and Space Chemistry, 3(10)

ISSN
2472-3452

Authors
Mangiante, D
Schaller, RD
Banfield, JF
et al.

Publication Date
2019-10-17

DOI
10.1021/acsearthspacechem.9b00169

Peer reviewed

Pathways for the Photoreduction of Fumarate on ZnS

David Mangiante,[†] Richard D. Schaller,[‡] Jillian F. Banfield,[†,§] and Benjamin Gilbert[*,§]

[†] Department of Earth and Planetary Sciences, University of California Berkeley, Berkeley, California 94720, United States [‡] Center for Nanoscale Materials, Argonne National Laboratory, Lemont, Illinois 60439, United States [§] Energy Geoscience Division, Lawrence Berkeley National Laboratory, Berkeley, California 94720, United States

Corresponding Author *E-mail: bgilbert@lbl.gov

Abstract

Semiconductor mineral particles can act as photocatalysts for organic redox reactions that occur enzymatically in modern biological metabolic pathways. Semiconductor mineral-mediated photocatalysis may have contributed to the prebiotic synthesis of organic acids on the early Earth, but assessing the plausibility of this hypothesis is impeded by the lack of knowledge about the mechanisms for light-driven organic redox reactions on mineral surfaces. We selected one step in the reverse tricarboxylic acid (rTCA) cycle, the reduction of fumarate to succinate, that has been shown to be photocatalyzed by zinc sulfide (ZnS). Using static and time-resolved optical emission and absorption spectroscopy, we studied the adsorption of fumarate and the rates and pathways for charge transfer. We find that ZnS transfers photoexcited electrons to bound and dissolved fumarate on a wide range of time scales but not to succinate, supporting the concept that ZnS mediated photoreduction of fumarate could have operated in oceans of the early Earth. Optical transient absorption (TA) spectroscopy identified a signature tentatively attributed to the fumarate radical anion that is stable for at least 8 ns, providing evidence that fumarate photoreduction under solar illumination levels occurs by successive photoelectron transfer. The model for electronic excitation, relaxation, and interfacial charge-transfer processes in ZnS provided here will inform all future studies of the photochemical reactions of this mineral.

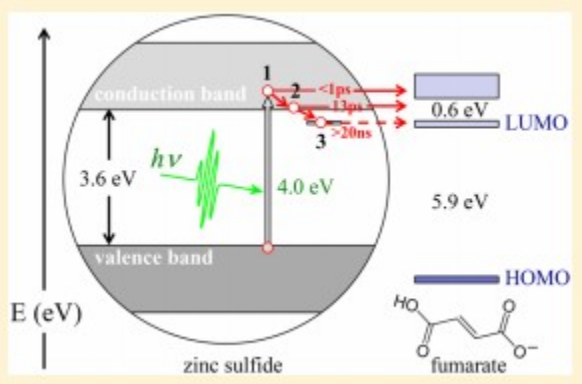

KEYWORDS: Photochemistry, Carbon cycle, Carbon dioxide, Mineralization, Ultrafast spectroscopy

Introduction

One scenario for the origin of life suggests that abiotic reactions first generated the organic molecules that participate in core metabolic pathways observed in modern organisms.(1) Much attention has been given to the tricarboxylic acid (TCA) cycle, which in the forward direction couples the respiration of organic molecules to the production of chemical energy in the form of adenosine triphosphate (ATP).(2) Certain bacteria employ a reverse TCA cycle, which consumes energy and builds longer-chain organic acids through the addition of CO_2. Thus, an abiotic reverse tricarboxylic acid (rTCA) cycle could be a mechanism for prebiotic synthesis of organic precursors of complex biomolecules.

Semiconductor minerals present on the early Earth may have served as the catalyst for the photochemical generation of prebiotic molecules. It is widely accepted that the early Earth was characterized by reducing conditions and that hydrothermal vents supplied H_2S and metals including Zn to the oceans,(3) a process that in modern oceans leads to the precipitation of zinc sulfide (ZnS).(4) Martin and co-workers have shown that ZnS can act as a photocatalyst and promote many steps in the rTCA cycle.(5,6) Observed reactions include 3 out of 5 reduction steps of the rTCA cycle, including exergonic steps requiring both light-driven oxidation and reduction, such as the conversion of pyruvate to α-ketoglutarate.(7−10) Parallel research in the field of solar energy conversion has shown that ZnS and other metal chalcogenide semiconductors can perform a large number of photochemical reactions including the reduction of CO_2.(11−13) Recently, Zhou and Guzman studied the two-electron reduction of fumarate to succinate (Scheme 1), seeking to establish the mechanism of heterogeneous excited-state charge-transfer reactions on ZnS.(14) They measured the yield of the reaction across a range of solution pH values and under periodic illumination, chopping the excitation over a range of frequencies (approximately 1 Hz to 0.1 mHz). They developed a conceptual model of the elementary steps consistent with their observations, although they did not obtain direct evidence for the electronic states and intermediate species that were proposed.

Scheme 1. Reduction of Fumarate to Succinate

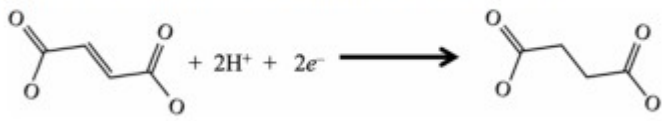

Time-resolved spectroscopic methods can complement traditional studies of reaction kinetics by identifying the signatures and measuring the lifetimes of reaction intermediates (e.g., ref (15)). We applied ultrafast optical absorption

and fluorescence spectroscopy to characterize the excited electronic states of ZnS that participate in the reduction reaction and measured the lifetimes of these states with and without fumarate or succinate. This work provides the most detailed view of the electronic states in ZnS that we find to participate in light-promoted interfacial electron transfer. We further elucidated the pathways and time scales for the first electron-transfer step in the reduction of fumarate. We provide optical spectroscopic evidence for the surface-stabilized fumarate radical anion proposed by Zhou and Guzman,(14) but we show that this intermediate is created on an ultrafast (sub-100 ps) time scale not the ~300 μs time scale previously suggested.

We performed ultrafast mid-infrared (mid-IR) spectroscopy with the goal of observing the protonation states of reduced fumarate. We find, however, that transient mid-IR absorption of fumarate on semiconductor nanoparticles is overwhelmed by the mid-IR absorption of electrons photoexcited to the conduction band (CB). Nevertheless, the mid-IR data provide an independent measurement of the rate of interfacial charge transfer from ZnS to fumarate. This study contributes an improved conceptual model for the way a two-electron organic reduction reaction proceeds via sequential one-electron light-promoted reduction.

Materials and Methods

ZnS Nanoparticle Synthesis and Characterization

ZnS Synthesis

We used a published method shown to synthesize ZnS nanoparticles without quantum confinement effects on optical excitation.(8) ZnS was precipitated by adding 80 mL of 50 mM $Na_2S·9H_2O$ dropwise to 70 mL of 50 mM $ZnCl_2$ while stirring. The resultant milky white suspension was kept for about 1.5 days at 30 °C before centrifugation to exchange supernatant solution with 1 mM Na_2S solution that can serve as a scavenger of valence-band holes and trace O_2.(8,16) Solution exchange was repeated three times to yield a particle concentration of about 7.5 g/L. All synthesis steps were performed in the anaerobic glovebox apart from centrifugation, and the product was stored anaerobically in sealed opaque containers.

ZnS Characterization

Low-resolution transmission electron microscopy indicated the sample to contain aggregates of sub-10 μm primary particles. We performed X-ray diffraction (XRD) to confirm the purity of the product and to estimate the nanoparticle size. We used the full-profile refinement software MAUD,(17) and using the crystallographic structure for sphalerite (*cubic* ZnS), we found the mean particle size to be 6.4 ± 4 nm. The surface area of ZnS nanoparticles was measured to be 170–200 m^2/g among batches using the BET method to obtain an adsorption isotherm of nitrogen. As-synthesized ZnS plus excess Na_2S at high pH had a zeta potential of approximately −40 mV in agreement with prior studies.(5,13)

Fumarate Adsorption to ZnS

We quantified the affinity of fumarate to ZnS under the same conditions as the photoreduction experiments. We added varying quantities of 10 mM fumarate and 2 M HCl or 4 M NaOH to 1 mL aliquots of ZnS, equilibrated overnight, and recorded the pH with a Mettler Toledo InLab Micro pH electrode. The suspensions were then centrifuged at 13 krpm for 20 min to remove ZnS. Centrifugation removed the vast majority of ZnS, but background absorption by residual dispersion of individual nanoparticles interfered with the quantitation of fumarate. This residual was dissolved by the addition of 0.1 mL of concentrated HCl. The concentration of dissolved fumarate was quantified by UV–vis absorption at 220 nm (Ocean Optics) with reference to a calibration curve.

Liquid Chromatography Mass Spectrometry (LCMS)

We used a LCMS workflow(18) to follow the ZnS catalyzed transformation of fumarate to succinate by ultraviolet light in pH 5 solutions using a Xenon arc lamp (Oriel). Suspensions of ZnS and fumarate exposed to light were centrifuged at 13 krpm for 10 min to remove ZnS. The supernatant solution was removed, lyophilized, and reconstituted in 95% acetonitrile and 5% water. This solution was passed through a Waters hydrophilic interaction chromatography (HILIC) column, a well established method for separating small anionic organic metabolites.(19) The solution was nebulized in negative mode, and solute mass-to-charge ratios were measured on an Agilent 6520 QTOF.

Fluorescence Spectroscopy Measurements

We performed conventional (time-integrated) fluorescence emission spectroscopy to investigate quenching of ZnS fluorescence by fumarate and time-resolved fluorescence studies to quantify the lifetimes of redox-active excited states.(20)

Fluorescence Quenching Measurements

The fluorescence signal from a semiconductor will be reduced (quenched) if electrons or holes are transferred to an acceptor species before recombination and photon emission.(21) Thus, the observation of fluorescence quenching is a good indicator of interfacial redox processes, although nonredox active species can reduce the fluorescence intensity by other mechanisms. We used a Fluorolog II spectrometer (Horiba, Japan) to measure fluorescence emission spectra from suspensions of ZnS in pH 5 or pH 10 aqueous solutions at a mineral concentration of 2 g/L with added fumarate or succinate in a 10 mm path length quartz cuvette. We used a 310 nm excitation wavelength and a 350–700 nm emission scan range. An additional fluorescence quenching experiment was performed with methanol as solvent instead of water.

Fluorescence Lifetime Measurements

We used a streak camera to capture the time-dependent fluorescence spectra from 0 to 120 ps following photoexcitation of ZnS with pulsed 310 nm excitation, using the same amplified femtosecond Ti:sapphire laser system described below, and a 300–750 nm excitation wavelength range. Two suspensions were studied: ZnS at a concentration of 250 mg/L and at pH 5 with 0.5 mM sodium sulfide with or without fumarate at 2.5 mM. Fluorescence lifetime plots were obtained by integrating the emitted intensity from 400 to 600 nm, excluding sharp peaks centered at time zero caused by scatter from the excitation beam. By fitting Gaussian profiles to these peaks, we determined the instrument response to be 4.9 ps. The fluorescence lifetime was quantified by fitting an exponential decay to each data set of the form $I(t) = I_0 + I_{120} \exp(-t/\tau)$, where I_0, I_{120}, and τ were fit parameters.

Optical Transient Absorption Spectroscopy

Optical transient absorption (TA) spectroscopy reveals how the UV–vis spectrum of a material or species changes during a light-driven process. TA spectroscopy has been used to follow electron-transfer processes in many semiconductor particles and organic molecules.(22−24)

Data Acquisition

We performed TA spectroscopy with a 310 nm pump and UV–visible (UV–vis) spectrophotometer at the Argonne Center for Nanoscale Materials (CNM) using an amplified femtosecond Ti:sapphire laser system at 2 kHz repetition rate. A small amount of the laser output is used to generate the white light continuum probe. The remaining 800 nm power pumps an optical parametric amplifier (OPA) to produce the excitation pulses. The two outputs then enter a transient absorption spectrometer (Helios, Ultrafast Systems), where the probe is variably delayed relative to the pump by increasing the path length using a translating mirror. A UV–vis spectrograph is used to collect the spectral content of the probe from 440 to 760 nm as a function of delay (limited to a maximum delay of 7.8 ns). The overall time resolution was 100 fs as inferred from the cross-phase modulation during temporal overlap of the pump and probe pulses. The OPA generated a small amount of unwanted frequency-doubled light that contributed an artifact at 400 nm.

Typical samples consisted of 50 mL aqueous suspensions containing 250 mg/L ZnS, 2.5 mM fumarate or succinate, and 0.5 mM sodium sulfide. Samples were circulated through a 2 mm path length quartz flow-cell cuvette and irradiated with 310 nm light at powers of 50–300 μW and a spot diameter of 250 μm. The signal response was linear in this power range, and the reported data was acquired with 200 μW illumination.

Data Processing

The optical TA data were processed and analyzed using custom routines in IgorPro software. First, the data were dechirped to correct for wavelength-dependent differences in the speed of light propagation through the sample.

Second, a baseline spectrum (an average of the 5 transient spectra prior to photoexcitation) was subtracted from all spectra. This correction successfully removed the artifact centered at 400 nm.

Multiwavelength Kinetics Analysis

We extracted transient kinetics traces at 16 wavelengths between 350 and 700 nm and used a linear least-squares fitting method to simultaneously fit all the traces as a sum of a predetermined number of exponentially decaying transient spectra. This analysis finds the decay time constants, τ_i, and the spectrum amplitudes at each wavelength, $a_i(\lambda)$, that reproduce the time-dependent TA signal:

$$\mathrm{TA}(\lambda, t) = \sum_i a_i(\lambda) \exp(-t/\tau_i) \quad (1)$$

The plot of the relative amplitudes, i.e., the a_i's, reveals the line shape of the contributing intermediate species. The analysis of all samples contained a negative transient contribution with a subpicosecond time constant. This contribution was assumed to be an effect of stimulated emission (in which the probe pulse stimulates fluorescence emission from an excited state). Because this process is not relevant to the photochemical processes studied here, it was fitted but is not reported or discussed further below.

ZnS Nanoparticle Photoexcitation Calculations

The laser pulses used in the TA studies can deliver a higher photon flux density than solar radiation at the Earth's surface. Therefore, we calculated the mean number of photoexcitation events per ZnS nanoparticle per pulse, $\langle N \rangle$, to ensure that we remained in the single excitation regime. The absorption of light by a nanoparticle is determined by both the optical properties of the intrinsic material and the extent of light scattering from the object.(25) Thus, the absorption cross section for a semiconductor nanoparticle, σ, is given by


(2)

where n refers to the index of refraction, V is the particle volume, and α_{ZnS} is the bulk absorption cross section. The shape function is given by

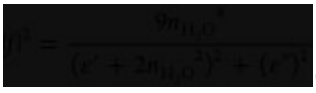
(3)

where ε′ and ε″ are the real and imaginary parts of the dielectric constant. Using literature values for the optical properties for *cubic* ZnS at 310 nm given in Table S1,(26,27) we calculate the absorption cross section for a 6 nm particle to be 8.7×10^{-16} cm^2. For a photon flux density, j, the mean number of absorption events per second $\langle N \rangle = j\sigma$. For our experimental conditions, absorption by ZnS appreciably reduced the photon intensity as the laser pulse traversed the 2 mm cuvette. Thus, we numerically calculated

⟨*N*⟩ as a function of distance as reported in Figure S1. The calculations show that ⟨*N*⟩ ~ 1 for the highest laser power used in this study.

Midinfrared Transient Absorption Spectroscopy

We use the same amplified femtosecond Ti:sapphire laser system described above with a 128-element HgCdTe mid-infrared array detector to acquire transient mid-IR data as a function of pump–probe delay. Because of the very high absorption of mid-IR by water, these experiments were performed using methanol or isopropanol as the solvent.

Results

Fumarate Adsorption

We studied the adsorption of fumarate to ZnS, finding a strong dependence on solution pH. We first acquired an absorption isotherm of fumarate on ZnS nanoparticles at pH 5, which was adequately fitted by a Langmuir-type model as used for arsenate sorption on sphalerite (Figure S2).(28) We then characterized the pH dependence of fumarate sorption by measuring the surface coverage as a function of pH in solutions containing the quantity of fumarate required for 50% surface saturation. As shown in Figure 1, the sorption extent ranged from completely unbound at pH 10 to fully adsorbed at pH 5. The trend confirms the conclusion that fully protonated and singly deprotonated fumarate species sorb to ZnS but the doubly deprotonated species does not bind.(14)

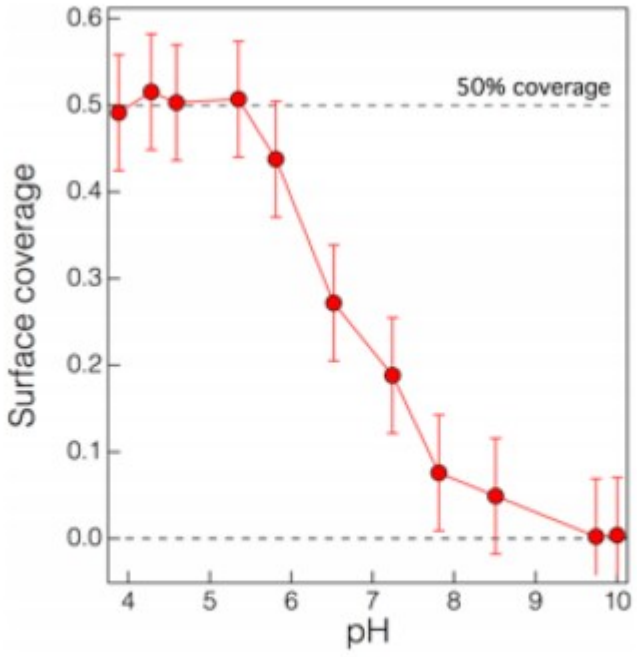

Figure 1. pH dependence of the sorption of fumarate to ZnS. Below pH 5.4, all added fumarate was surface bound.

Photoreduction of Fumarate to Succinate

We used liquid chromatography coupled to time-of-flight mass spectrometry (LC-MS) to verify that the ZnS nanoparticles were catalytically active. For 5 mL suspensions of ZnS plus fumarate at pH 5, the LC-MS data (Figure S3) showed the reaction to be completed after about 2 h of continuous illumination from a mercury arc lamp with succinate to be the sole product.

Fluorescence Quenching

We acquired fluorescent emission spectra of ZnS nanoparticles with continuous 310 nm excitation in pH 5 solutions with fumarate at a range of concentrations (0.08 to 10.0 mM), with succinate (2.0 mM), or with no organic acid. As shown in Figure 2, succinate caused little change to the fluorescence signal, indicating that photoexcited ZnS does not transfer (or accept) an electron to (or from) succinate. In contrast, fumarate caused a concentration-dependent drop in the signal, a quenching response that is consistent with a photoreduction process. We used the adsorption isotherm for fumarate binding to ZnS at pH 5 (Figure S2) to estimate the fumarate surface coverage for all the fumarate concentrations used in the fluorescence quenching study. As shown in the inset, this calculation revealed that the fluorescence quenching of ZnS is linearly proportional to the coverage of fumarate on the surface. This is strong evidence of a mechanism in which photoexcited electrons are transferred to bound species and not to freely diffusing molecules.(29)

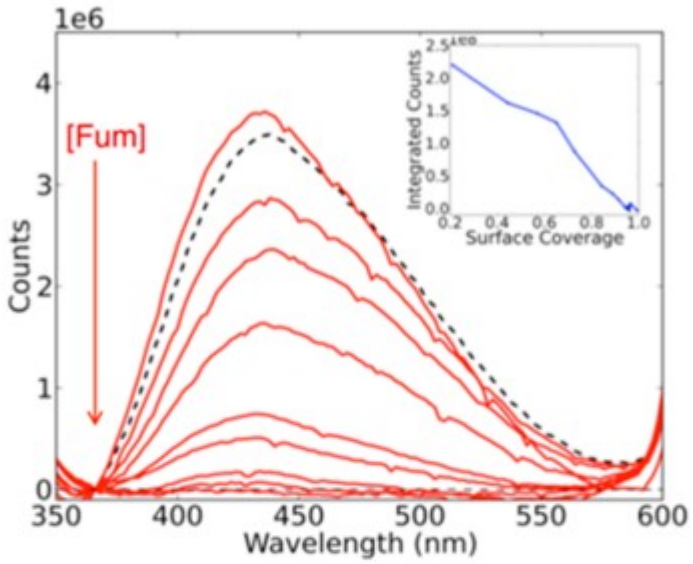

Figure 2. Fluorescence emission spectra (red solid lines) acquired with a 310 nm excitation wavelength, showing quenching of ZnS nanoparticle fluorescence by added fumarate (0.01 to 10.0 mM). The black dashed line is the fluorescence in the presence of 2.0 mM succinate. Inset: Plot of integrated ZnS fluorescence counts versus fumarate adsorption showing a linear drop in fluorescence with surface coverage. The adsorption isotherm used to generate this plot is given in Figure S2.

Successive fluorescence emission scans on the same sample showed a rebound of intensity that returned asymptotically to the unquenched signal with exposure time (Figure S4). For 2.0 mM fumarate, complete restoration of fluorescence was observed after 20 min. The recovery of the fluorescence signal indicates that ZnS photoexcitation irreversibly transfers electrons to surface bound fumarate, generating a reduced product that cannot further quench the fluorescence. In high pH solutions in which fumarate does not bind, we also observed partial fluorescence quenching (Figure S5A). This indicates that electron transfer can occur between ZnS nanoparticles and freely diffusing unbound fumarate molecules. Prior to time-resolved vibrational spectroscopy studies in methanol, we compared the fluorescence of ZnS in methanol with and without fumarate. Fumarate completely quenched ZnS fluorescence in methanol (Figure S5B), indicating that the fumarate photoreduction pathway is active in this solvent.

Fluorescence Lifetime

Figure 3 compares fluorescence lifetime data for ZnS with and without fumarate. For ZnS nanoparticles alone in water, photoexcitation caused prompt fluorescence emission (within the temporal resolution of the experiment, ~4.3 ps) and the intensity decayed with a single exponential time constant over ~100 ps, as observed previously.(30) The residual

fluorescence observed at the end of the measurement window is consistent with there being another longer time scale for recombination, which we also observed in optical TA studies (below) and was previously reported for ZnS.(31,32)

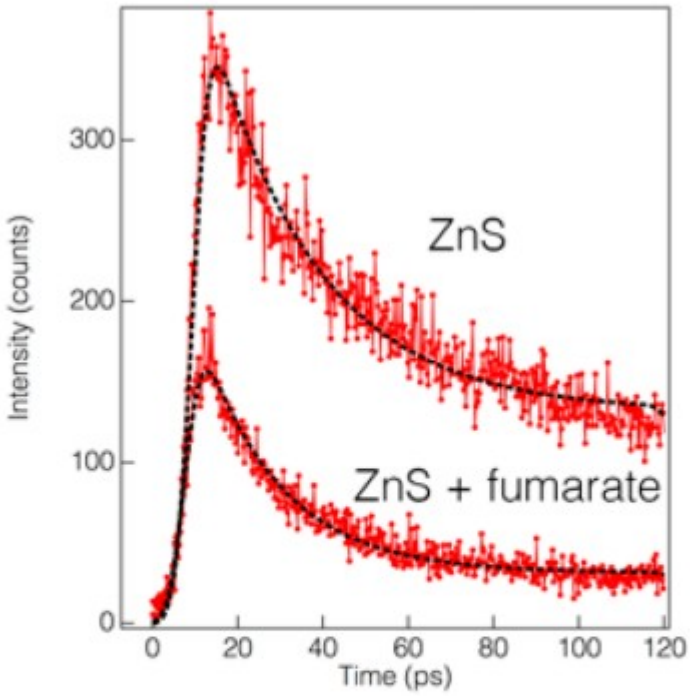

Figure 3. Fluorescence lifetime measurements for the same concentration of ZnS nanoparticles with and without fumarate. The data (red markers) were fitted (black lines) by a single exponential plus a constant offset that was convolved with 4.3 ps Gaussian to account for the instrument response.

The emission from the sample containing a fixed concentration of ZnS but with added fumarate showed approximately half the initial intensity, decayed more rapidly and to a smaller residual signal at 120 ps. The faster decay rate in the presence of fumarate is consistent with the introduction of an additional mechanism that competes with the fluorescent pathway for photoexcited electrons or holes. We infer the additional process to be interfacial electron transfer to fumarate and use the comparison of the decay rates with and without fumarate to estimate the rate of transfer.(33) The time constant, τ_{total}, observed in the presence of two pathways is given by

$$1/\tau_{total} = 1/\tau_F + 1/\tau_{ET} \quad (4)$$

where τ_F is the rate of the fluorescent decay of ZnS and τ_{ET} is the rate of electron transfer. We fitted the fluorescence decay kinetics for ZnS with and without fumarate using a single exponential decay plus a constant offset that accounted for the long-lived signal. Using eq 4 and the best-fit values given

in Table1, we obtain a time constant for electron transfer to fumarate of 13 ps.

Table 1. Best-Fit Fluorescence Lifetimes

sample	τ (ps)[a]	I_0 (counts)[b]	I_{120} (counts)[b]
ZnS	29.0 ± 0.4	266	126
ZnS + fumarate	18.5 ± 0.1	174	32

[a]The errors are the standard deviations on the best-fit values. [b]The peak and residual fluorescence intensities at 0 and 120 ps, I_0 and I_{120}, were obtained from the fitting and have an uncertainty of 1−2 counts.

Optical Transient Absorption (TA) Spectroscopy

We acquired TA data from ZnS suspensions (1) with and without fumarate and (2) at pH 10 and pH 5. Representative kinetics traces at 475 nm from the TA data are given in Figure S6. For one sample, ZnS alone at pH 5, the data quality was significantly worse than for all others and it was visually evident that this was due to nanoparticle aggregation. Thus, we present below a comparison of ZnS plus fumarate at pH 5 (fumarate bound) and pH 10 (unbound).

ZnS Plus Fumarate TA at pH 10

Figure 4A shows the TA spectra for ZnS with unbound fumarate at pH 10 at 0.5 ps, 10 ps, and 1 ns after photoexcitation and overlays these spectra with the ZnS ground-state UV–vis absorption spectrum. The TA spectra contain two principal contributions shortly after excitation.

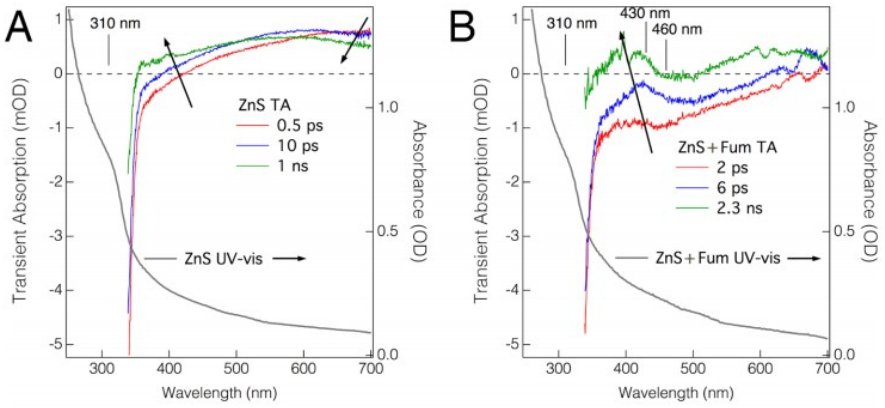

Figure 4. Optical transient absorption (TA) spectra from ZnS plus fumarate at pH 10 (A; fumarate unbound) and pH 5 (B; fumarate bound). The TA spectra are generated by subtracting the ground-state UV−vis spectrum of the sample from the spectrum acquired at the indicated times after excitation at 310 nm. The ground-state absorbance spectra are plotted against the right axis in units of optical density (OD) and the difference spectra, against the left axis in units of milli OD (mOD). Arrows indicate the evolution of the TA spectra with time.

Negative Component below ~360 nm

The negative line shape at low wavelength mirrors the ground-state absorption and thus represents a loss (bleaching) of this absorption. It occurs because a valence band (VB) electron excited to the conduction band (CB) strongly suppresses the probability for a second photoexcitation event. The ground-state bleach can be interpreted as a direct measurement of electrons at the bottom of the CB.

Positive Component above ~360 nm

The positive response at higher wavelength is a new absorption band that extends into the infrared region. Broad, long-lived excited-state absorption features are frequently observed in optical TA data for semiconductors. They are attributable to excited-state electrons situated either at the bottom of the CB or in localized trap states that can undergo further optical excitations.

Figure 4A clearly shows that both the bleach and the new absorption band decayed with time after photoexcitation. However, a comparison of the kinetics at the appropriate wavelengths (Figure 5) shows that the rates of decay are not identical, indicating that electron–hole recombination is not the dominant process. Approximately 80% of the bleach is lost at 8 ns, while more than 50% of the excited-state absorption signal persists beyond this time. The reappearance of band gap excitations before the system has returned to the ground state indicates that electrons at the bottom of the CB have transferred to other states that do not suppress additional photoexcitation. As discussed below, these states are likely to be mid-band-gap trap states.

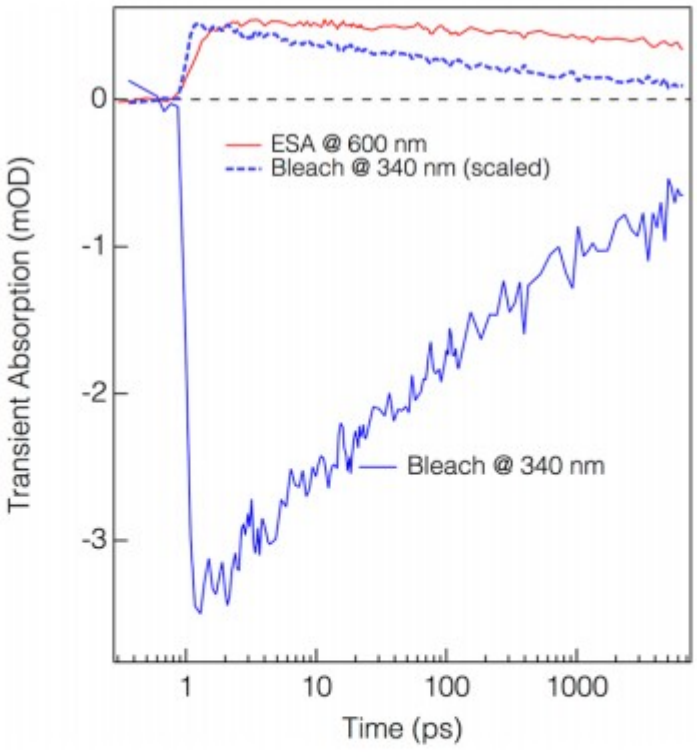

Figure 5. Transient absorption kinetics traces from ZnS nanoparticles (without fumarate) at 340 nm (dominated by the ground-state bleach) and at 600 nm (dominated by new excited-state absorption (ESA) intensity). A copy of the 340 nm bleach trace (dashed line) has been multiplied by −1 and rescaled to show that the loss of the bleach occurs faster than the loss of the ESA. The data were shifted on the time axis to place the laser pump time point at 1 ps to enable the data to be plotted on a logarithmic time axis.

To further examine the electron processes in ZnS with unbound fumarate, we extracted kinetics curves at 15 wavelengths (from 350 to 750 nm) and used a nonlinear least-squares global fitting approach to identify spectra that evolved with distinct exponential decay constants. The fits are given in Figure S7. We obtain three distinct spectral components that are labeled in Figure 6A according to their attribution. The bleach signal and the conduction-band electron signal exhibit similar kinetics with two characteristic time constants (9 and 250 ps). At longer times, the TA spectra are dominated by a narrower, higher-energy, and excitation feature that is consistent with a trapped state with an energy beneath the bottom of the CB. Thus, we conclude that CB electrons are localized into midgap trap states on 9 and 250 ps time scales. The lifetime of the trapped-electron state exceeded the experimental time window and is estimated to be approximately 20 ns.

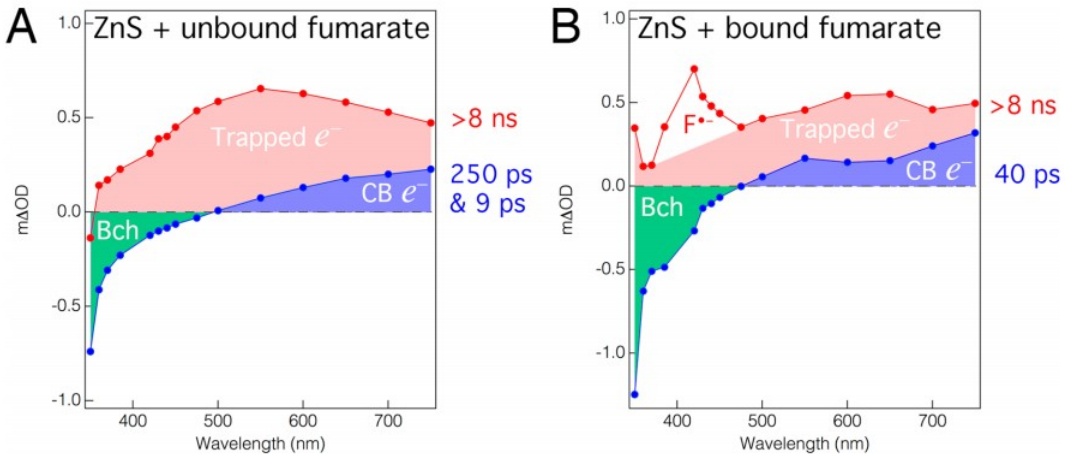

Figure 6. Component transient optical absorption spectra obtained from multiwavelength fitting of the optical TA data for ZnS plus fumarate at (A) pH 10, fumarate unbound and (B) pH 5, fumarate bound. As described in the text, the transient spectra that decay on sub-ns time scales (blue markers) have contributions from conduction band electrons (CB e^-) and ground state bleach (Bch). The longer-lived transient spectra (red markers) have contributions from trapped electrons and, when fumarate is bound, a signal tentatively attributed to the fumarate radical anion ($F^{\bullet-}$). The kinetics curves from which these spectra were extracted are reported in Figure S7.

ZnS Plus Fumarate TA at pH 5

Figure 4B shows the TA spectra of ZnS with bound fumarate at pH 5. These data show the strong bleach signal below ~350 nm that was seen in all ZnS samples but also show much less absorption intensity in the wavelength range that is attributed to electrons in trap states. In addition, a new absorption feature around 400–490 nm appeared within a few ps and persisted until the longest time. Component TA spectra were extracted using the multiwavelength kinetics analysis of the data and are presented in Figure 6B. These data suggest that far fewer electrons reach trap states in ZnS and instead cause the formation of a new species within a few picoseconds after photoexcitation. As discussed below, the new species is interpreted as the one-electron reduction product of bound fumarate.

Midinfrared Transient Absorption Spectroscopy

The mid-IR TA data for suspensions of ZnS nanoparticles were dominated by a strong and broad excited-state absorption signal that extended through the entire wavelength range investigated during these studies (4–7 μm; 2500–1430 cm^{-1}) (Figure 7A) and decayed on a subpicosecond time scale (Figure 7C) that was quantified by fitting (Table2). These fast dynamics are interpreted as optical absorption by “hot” electrons during relaxation to the bottom of the CB. The residual signal after the first picosecond decays more slowly and is completely lost within ~300 ps. This is the same time scale over which the signal from trapped electrons becomes evident in the optical TA data (Figure 6), and thus, we conclude that the optical and mid-IR data record the same electron-trapping process.

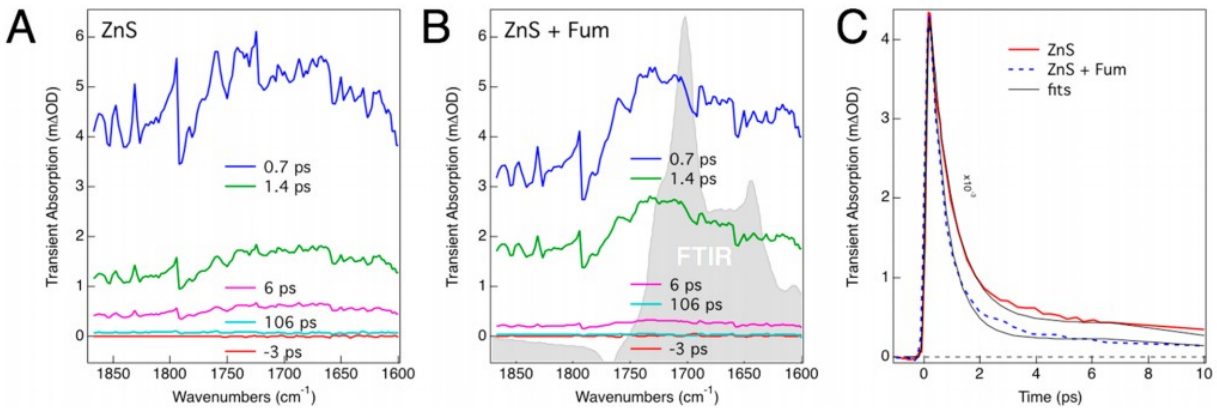

Figure 7. Midinfrared (mid-IR) transient absorption spectra acquired from the same concentration of ZnS nanoparticles without (A) or with (B) fumarate in methanol suspensions at selected time points before or after photoexcitation. Gray shaded data shows the ground-state FTIR spectrum from ZnS plus fumarate sample prior to TA. The major peak is the C═O vibration. (C) Kinetics traces at 5.8 μm (1724 cm^{-1}) from ZnS nanoparticles (red line) and ZnS plus fumarate (blue dashed line).

Table 2. Best-Fit Mid-IR Transient Decay Kinetics[a]

sample	τ (ps) at 1724 cm^{-1} [b]	τ (ps) at 1818 cm^{-1} [c]
ZnS	0.77 ± 0.1	0.77 ± 0.1
ZnS + fumarate	0.58 ± 0.1	0.55 ± 0.2

[a]Reported are the time constants for a single stretched exponential decay with $\beta = 0.9$ and with the fit convolved with a 0.12 ps Gaussian response function. [b]On the fumarate $\nu_{C=O}$ resonance. [c]Off resonance.

In the presence of adsorbed fumarate or succinate, the mid-IR TA spectra resembled the ZnS-only data with an additional feature (Figure 7B) at the position of the ground state $\nu_{C=O}$ vibration(34) (cf. Figure S8). However, this feature exhibited identical dynamics to the response away from resonance, indicating that it was not a vibrational signature of fumarate redox chemistry. Throughout the wavelength region probed, no new molecular vibrational features could be detected. We concluded that the experimental system was not sufficiently sensitive to changes in surface molecules and that the mid-IR data only provided information on the electronic excitations in the semiconductor particles. Time-resolved electron paramagnetic resonance (EPS) spectroscopy may be an alternative approach to characterize the oxidation and protonation states of the fumarate radical. (35) Nevertheless, the mid-IR data revealed an additional ultrafast pathway for fumarate reduction because the decay rate was significantly faster in the presence of surface-bound fumarate (Table2). This observation indicates that photoexcited electrons can transfer to and reduce fumarate before relaxation to the bottom of the CB.

Discussion

ZnS Photoexcitation

The spectroscopic studies identify three excited states in ZnS that are populated by electrons following light absorption and relaxation. The 310 nm excitation excites VB electrons into the CB (state 1) creating a strong mid-IR signal that is rapidly lost as the electron relaxes to the bottom of the CB (state 2). Electrons at the bottom of the CB reduce the band gap absorption intensity (i.e., cause bleaching) but subsequently transfer to a trap state (state 3) on at least one sub-ns time scale. Electrons in this trap state do not cause excitation bleaching. Recombination from this trap state occurs through fluorescence emission with a lifetime estimated to be 20 ns. Figure 8 shows a scheme that illustrates states 1–3 and the electron excitation, relaxation, and interfacial-transfer processes for bare ZnS and for the first electron reduction of fumarate. The position of the calculated molecular orbital energy levels of fumarate(36) relative to the electronic states of ZnS is unknown. However, the fast interfacial electron-transfer rates suggest a close energy alignment as proposed in Figure 8. Because we calculated the ZnS photoexcitation efficiency to be less or equal to one exciton per nanoparticle and because we verified experimentally a linear dependence of signal strength on laser power, the results are relevant to single-electron photochemical reactions expected under solar illumination.

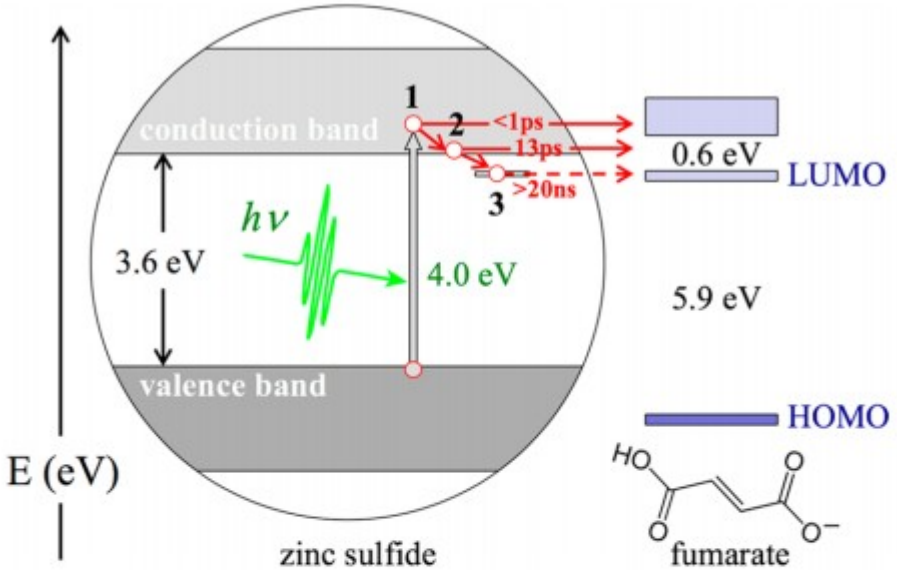

Figure 8. Proposed energy-level diagram showing the electron excitation, relaxation, and interfacial-transfer processes for the first electron reduction of fumarate by photoexcited ZnS. The green arrow represents a photon of energy *hν*. Bold numbers **1**, **2**, and **3** label the excited electron states described in the text. Solid red arrows represent pathways for the ultrafast reduction of adsorbed fumarate that occur within 20 ps of photoexcitation. The dashed red arrow represents a pathway for fumarate reduction from a trap state with a lifetime much greater than 1 ns that can reduce dissolved and unbound fumarate. The molecular orbital energy levels for fumarate are taken from ref 36.

First Electron Reduction of Fumarate

Our data demonstrate that excited electrons in states 1 and 2 readily reduce bound fumarate and strongly indicate that electrons in state 3 can reduce dissolved fumarate. First, when fumarate is bound to ZnS, the fluorescence lifetime and mid-IR TA studies recorded lower signals within the first ~10 ps following photoexcitation compared to ZnS with unbound fumarate. This indicates that excited electrons can transfer to bound fumarate from state 1 before fully relaxing to the bottom of the CB. Second, the fluorescence lifetime and optical TA data both indicate that fumarate reduction by electrons in state 2 competes with electron trapping on a sub-100 ps time scale. Evidence that electrons lost from states 1 and 2 are transferred to bound fumarate is provided by the appearance of a new absorption feature in the optical TA data that we interpret to be the product of the one-electron reduction of bound fumarate (i.e., the fumarate radical anion). The line shape is located around 410 nm, which is red-shifted relative to the UV–vis absorption spectrum of the fumarate radical anion generated in water by pulse radiolysis.(37) However, our optical TA data below 400 nm are

increasingly dominated by the band gap absorption of ZnS, which may distort or obscure the lower wavelength portion of the transient molecular absorption. Finally, we observed a detectable loss of time-averaged fluorescence intensity in the fluorescence quenching experiments with and without fumarate at pH 10. Because fumarate does not bind to ZnS at pH 10, we infer that diffusion driven encounters between fumarate and ZnS enable electron transfer from the longest-lived states in the mineral, that is from state 3.

Using periodic illumination, Zhou and Guzman(14) identified two reaction time scales, ~300 μs and ~4.5 ms, that were interpreted, respectively, as the time scale for the first one-electron reduction and the time scale for the scavenging of valence-band holes by Na_2S. Our work, however, shows that the reduction of bound fumarate occurs on sub-10 ps and sub-100 ps time scales, and hence, an alternative interpretation of the ~300 μs time scale is required.

Second Electron Reduction and Succinate Formation

At low pH, the fumarate radical anion was stable (over 8 ns) when bound to the ZnS surface, and therefore, it is most likely that a second photoexcitation event reduces this intermediate to succinate. If reduced fumarate was to desorb, radical–radical disproportionation is a plausible mechanism for generating one succinate and regenerating one fumarate.(38,39) However, we are not aware of any observations of this pathway in the radical chemistry of fumarate (which is limited to reactions in homogeneous solutions). At high pH, we find evidence for the one-electron reduction of unbound fumarate, but Zhou and Guzman(14) observed a negligible yield of succinate.

Our observations are consistent with the interpretation that the addition of a second electron to the fumarate radical anion is less favorable than the first. The excess charge on the fumarate radical anion is likely to add an activation barrier for the second reduction step. At low pH, the excess could be compensated by protonation of a carboxylic acid group, but the charge densities are not likely to fully overlap. In this scenario, the state 3 sites that are the longest lived and the lowest in energy may be insufficiently reduced to complete the reaction. For both bound and unbound fumarate, it is, therefore, plausible that second-electron reduction is the rate-limiting step in the overall reaction.

Conclusions

This work elucidates the electronic states in ZnS that participate in the reduction of fumarate and likely in all photochemical reduction processes of this semiconductor. This work, together with the work of Zhou and Guzman, (14) highlights important chemical aspects of mineral photocatalysis of organic redox reactions. First, the sorption of molecules to the mineral surface not only enhances the rate of interfacial electron transfer by

removing transport limitations but also allows more reducing, but shorter lived, excited states to participate. Sorption, therefore, may be essential to overcome activation or thermodynamic barriers to electron transfer and is primarily determined by solution pH. Models for the composition of Archean oceans suggest that, despite the presence of high levels of atmospheric CO_2, the weathering of basalt seafloor(40) and continental silicates(41) provided a sink for CO_2 and a source of alkalinity leading to approximately pH 6.6 at 4.0 Ga. Under these conditions, a small but non-negligible fraction of available fumarate would associate to ZnS and be fully reduced. Second, organic redox reactions are two-electron processes that inevitably involve the formation of radical intermediates such as the fumarate radical anion. We have virtually no knowledge of the behavior and redox properties of such radical intermediates that are required for accurate models of mineral photocatalysis under different conditions including those proposed to be relevant to the early Earth. The application of time-resolved approaches that have sensitivity to organic molecule speciation and that can probe all relevant reaction time scales will be necessary to fill this knowledge gap.

Acknowledgments

This work was funded by the NSF Geobiology and Low-Temperature Geochemistry program under Grant No. 1324791. B.G. was supported by the Department of Energy (DOE), Office of Basic Energy Sciences (BES) under Contract No. DE-AC02-05CH11231. The use of the Center for Nanoscale Materials, an Office of Science user facility, was supported by the U.S. Department of Energy, Office of Science, Office of Basic Energy Sciences, under Contract No. DE-AC02-06CH11357.

References

1

Cody, G. D. Geochemical connections to primitive metabolism. *Elements* 2005, *1* (3), 139– 143,

2

Morowitz, H. J.; Kostelnik, J. D.; Yang, J.; Cody, G. D. The origin of intermediary metabolism. *Proc. Natl. Acad. Sci. U. S. A.* 2000, *97* (14), 7704–7708,

3

Mulkidjanian, A. Y. On the origin of life in the Zinc world: I. Photosynthesizing, porous edifices built of hydrothermally precipitated zinc sulfide as cradles of life on Earth. *Biol. Direct* 2009, *4*, 26,

4

Hsu-Kim, H.; Mullaugh, K. M.; Tsang, J. J.; Yucel, M.; Luther, G. W. Formation of Zn-and Fe-sulfides near hydrothermal vents at the Eastern Lau Spreading

Center: implications for sulfide bioavailability to chemoautotrophs. *Geochem. Trans.* 2008, *9* (1), 6,

5

Zhang, X. V.; Ellery, S. P.; Friend, C. M.; Holland, H. D.; Michel, F. M.; Schoonen, M. A. A.; Martin, S. T. Photodriven reduction and oxidation reactions on colloidal semiconductor particles: Implications for prebiotic synthesis. *J. Photochem. Photobiol., A* 2007, *185* (2–3), 301– 311,

6

Zhang, X. V.; Martin, S. T. Driving parts of Krebs cycle in reverse through mineral photochemistry. *J. Am. Chem. Soc.* 2006, *128* (50), 16032– 16033,

7

Guzman, M. I.; Martin, S. T. Photo-production of lactate from glyoxylate: how minerals can facilitate energy storage in a prebiotic world. *Chem. Commun.* 2010, *46* (13), 2265– 2267,

8

Guzman, M. I.; Martin, S. T. Prebiotic metabolism: production by mineral photoelectrochemistry of alpha-ketocarboxylic acids in the reductive tricarboxylic acid cycle. *Astrobiology* 2009, *9* (9), 833– 842,

9

Wang, W.; Li, Q. L.; Yang, B.; Liu, X. Y.; Yang, Y. Q.; Su, W. H. Photocatalytic reversible amination of alpha-keto acids on a ZnS surface: implications for the prebiotic metabolism. *Chem. Commun.* 2012, *48* (15), 2146– 2148,

10

Guzman, M. I.; Martin, S. T. Oxaloacetate-to-malate conversion by mineral photoelectrochemistry: implications for the viability of the reductive tricarboxylic acid cycle in prebiotic chemistry. *Int. J. Astrobiol.* 2008, *7* (3–4), 271– 278,

11

Horner, G.; Johne, P.; Kunneth, R.; Twardzik, G.; Roth, H.; Clark, T.; Kisch, H. Heterogeneous photocatalysis, part XIX - Semiconductor type A photocatalysis: Role of substrate adsorption and the nature of photoreactive surface sites in zinc sulfide catalyzed C-C coupling reactions. *Chem. - Eur. J.* 1999, *5* (1), 208– 217,

12

Kanemoto, M.; Shiragami, T.; Pac, C. J.; Yanagida, S. Semiconductor photocatalysis - effective photoreduction of carbon-dioxide catalyzed by ZnS quantum crystallites with low-density of surface-defects. *J. Phys. Chem.* 1992, *96* (8), 3521– 3526,

13

Zhou, R.; Guzman, M. I. CO2 Reduction under periodic illumination of ZnS. *J. Phys. Chem. C* 2014, *118* (22), 11649– 11656,

14

Zhou, R.; Guzman, M. I. Photocatalytic reduction of fumarate to succinate on ZnS mineral surfaces. *J. Phys. Chem. C* 2016, *120*, 7349– 7357,

15

Mangiante, D. M.; Schaller, R. D.; Zarzycki, P.; Banfield, J. F.; Gilbert, B. Mechanism of ferric oxalate photolysis. *ACS Earth and Space Chemistry* 2017, *1* (5), 270– 276,

16

Chakrapani, V.; Baker, D.; Kamat, P. V. Understanding the role of the sulfide redox couple (S2-/S-n(2-)) in quantum dot-sensitized solar cells. *J. Am. Chem. Soc.* 2011, *133* (24), 9607– 9615,

17

Lutterotti, L. Total pattern fitting for the combined size-strain-stress-texture determination in thin film diffraction. *Nucl. Instrum. Methods Phys. Res., Sect. B* 2010, *268*, 334– 340,

18

Bowen, B. P.; Northen, T. R. Dealing with the unknown: metabolomics and metabolite atlases. *J. Am. Soc. Mass Spectrom.* 2010, *21* (9), 1471– 1476,

19

Buszewski, B.; Noga, S. Hydrophilic interaction liquid chromatography (HILIC)—a powerful separation technique. *Anal. Bioanal. Chem.* 2012, *402* (1), 231– 247,

20

Lewis, N. S. An analysis of charge transfer rate constants for semiconductor/liquid interfaces. *Annu. Rev. Phys. Chem.* 1991, *42*, 543– 580,

21

Dorokhin, D.; Tomczak, N.; Velders, A. H.; Reinhoudt, D. N.; Vancso, G. J. Photoluminescence quenching of CdSe/ZnS quantum dots by molecular ferrocene and ferrocenyl thiol ligands. *J. Phys. Chem. C* 2009, *113* (43), 18676– 18680,

22

Sher, P. H.; Smith, J. M.; Dalgarno, P. A.; Warburton, R. J.; Chen, X.; Dobson, P. J.; Daniels, S. M.; Pickett, N. L.; O'Brien, P. Power law carrier dynamics in semiconductor nanocrystals at nanosecond timescales. *Appl. Phys. Lett.* 2008, *92* (10), 101111,

23

Nakato, T.; Watanabe, S.; Kamijo, Y.; Nono, Y. Photoinduced electron transfer between ruthenium-bipyridyl complex and methylviologen in suspensions of smectite clays. *J. Phys. Chem. C* 2012, *116*, 8562– 8570,

24

Wang, Y.-F.; Wang, H.-Y.; Li, Z.-S.; Zhao, J.; Wang, L.; Chen, Q.-D.; Wang, W.-Q.; Sun, H.-B. Electron extraction dynamics in CdSe and CdSe/CdS/ZnS quantum dots adsorbed with methyl viologen. *J. Phys. Chem. C* 2014, *118* (31), 17240– 17246,

25

Leatherdale, C. A.; Woo, W.-K.; Mikulec, F. V.; Bawendi, M. G. On the absorption cross section of CdSe nanocrystal quantum dots. *J. Phys. Chem. B* 2002, *106*, 7619– 7622,

26

Ozaki, S.; Adachi, S. Optical-constants of cubic ZnS. *Japanese Journal of Applied Physics Part 1-Regular Papers Brief Communications & Review Papers* 1993, *32* (11A), 5008– 5013,

27

Tsuchiya, T.; Ozaki, S.; Adachi, S. Modelling the optical constants of cubic ZnS in the 0–20 eV spectral region. *J. Phys.: Condens. Matter* 2003, *15*, 3717– 3730,

28

Bostick, B. C.; Fendorf, S.; Manning, B. A. Arsenite adsorption on galena (PbS) and sphalerite (ZnS). *Geochim. Cosmochim. Acta* 2003, *67* (5), 895– 907,

29

Becker, W. G.; Bard, A. J. Photoluminescence and photoinduced oxygen adsorption of colloidal zinc sulfide. *J. Phys. Chem.* 1983, *87*, 4888– 4893,

30

Smith, B. A.; Zhang, J. Z.; Joly, A.; Liu, J. Luminescence decay kinetics of Mn^{2+}-doped ZnS nanoclusters grown in reverse micelles. *Phys. Rev. B: Condens. Matter Mater. Phys.* 2000, *62* (3), 2021– 2028,

31

Dunstan, D. E.; Hagfeldt, A.; Almgren, M.; Siegbahn, H. O. G.; Mukhtar, E. Importance of surface reactions in the photochemistry of ZnS colloids. *J. Phys. Chem.* 1990, *94*, 6797– 6804,

32

Kanemoto, M.; Hosokawa, H.; Wada, Y.; Murakoshi, K.; Yanagida, S.; Sakata, T.; Mori, H.; Ishikawa, M.; Kobayashi, H. Semiconductor photocatalysis. 20. Role of surface in the photoreduction of carbon dioxide catalysed by colloidal

ZnS nanocrystallites in organic solvent. *J. Chem. Soc., Faraday Trans.* 1996, *92* (13), 2401– 2411,

33

Parsapour, F.; Kelley, D. F.; Craft, S.; Wilcoxon, J. P. Electron transfer dynamics in MoS_2 nanoclusters: Normal and inverted behavior. *J. Chem. Phys.* 1996, *104* (13), 4978– 4987,

34

Kang, S.; Xing, B. Adsorption of dicarboxylic acids by clay minerals as examined by in situ ATR-FTIR and ex situ DRIFT. *Langmuir* 2007, *23*, 7024–7031,

35

Bittl, R.; Weber, S. Transient radical pairs studied by time-resolved EPR. *Biochim. Biophys. Acta, Bioenerg.* 2005, *1707*, 117– 126,

36

Cotton, F. A.; Donahue, J. P.; Murillo, C. A.; Perez, L. M. Polyunsaturated dicarboxylate tethers connecting dimolybdenum redox and chromophoric centers: absorption spectra and electronic structures. *J. Am. Chem. Soc.* 2003, *125*, 5486– 5492,

37

Hayon, E.; Simic, M. Acid-base properties of radical-anions of *cis* and *trans* isomers. 1. fumarates and maleates. *J. Am. Chem. Soc.* 1973, *95* (8), 2433–2439,

38

Zard, S. Z. *Radical Reactions in Organic Synthesis*; Oxford University Press: Oxford, 2003.

39

Bielski, B. H. J.; Allen, A. O.; Schwarz, H. A. Mechanism of disproportionation of ascorbate radicals. *J. Am. Chem. Soc.* 1981, *103* (12), 3516– 3518,

40

Sleep, N. H. The Hadean-Archaean Environment. *Cold Spring Harbor Perspect. Biol.* 2010, *2* (6), a002527,

41

Krissansen-Totton, J.; Arney, G. N.; Catling, D. C. Constraining the climate and ocean pH of the early Earth with a geological carbon cycle model. *Proc. Natl. Acad. Sci. U. S. A.* 2018, *115* (16), 4105– 4110,